

Photon Structure Functions and Azimuthal Correlations of Lepton Pairs in Tagged $\gamma\gamma$ Collisions

The L3 Collaboration

Abstract

The reactions $e^+e^- \rightarrow e^+e^-e^+e^-$ and $e^+e^- \rightarrow e^+e^-\mu^+\mu^-$, in a single tag configuration, are studied at LEP with the L3 detector. The data set corresponds to an integrated luminosity of 93.7 pb^{-1} at $\sqrt{s} = 91 \text{ GeV}$. Differential cross sections are measured for $1.4 \text{ GeV}^2 \leq Q^2 \leq 7.6 \text{ GeV}^2$. The leptonic photon structure function F_2^γ and azimuthal correlations are measured for $e^+e^- \rightarrow e^+e^-\mu^+\mu^-$. The related structure functions F_A^γ and F_B^γ , which originate from interference terms of the scattering amplitudes, are determined for the first time.

Submitted to *Phys.Lett. B*

1 Introduction

The reaction $e^+e^- \rightarrow e^+e^-l^+l^-$, where l can be any charged lepton, arises from $O(\alpha^4)$ QED processes [1]. Usually the scattered electrons are undetected; the analysis of this configuration has been published in [2]. In this paper we study the single tag configuration, where one of the scattered electrons is measured. This reaction is treated as an electron-photon deep inelastic scattering process; it provides not only a test of QED but also a check of the experimental procedures adopted in the analysis of the hadronic photon structure functions.

Using data collected from 1991 to 1994 with the L3 detector at LEP, with a beam energy $E_{beam} \simeq 45.6$ GeV, we investigate the reactions:

$$e \gamma^* \rightarrow e e^+ e^-,$$

$$e \gamma^* \rightarrow e \mu^+ \mu^-,$$

where the three final state leptons are detected. The measurement of the scattered electron determines the four-vector of the radiated virtual photon, which is the probe photon. The target virtual photon, γ^* , radiated by the unobserved electron, is almost real. Three leptonic photon structure functions F_2^γ , F_A^γ and F_B^γ , related to different helicity states of the colliding photons, are extracted from the measured cross sections for $e \gamma^* \rightarrow e \mu^+ \mu^-$. At LEP, the leptonic structure function F_2^γ has been measured previously [3, 4] and the ratio F_B^γ/F_2^γ was extracted from azimuthal correlations [5].

2 Formalism

The lowest order Feynman diagrams which describe the reactions $e^+e^- \rightarrow e^+e^-l^+l^-$ involve several processes classified as multiperipheral, annihilation, bremsstrahlung and conversion [2]. The dominant contribution is the multiperipheral diagram, which includes the interaction of two virtual photons. Annihilation and bremsstrahlung contributions become important only for small effective masses of the produced lepton pair. The incoming beam electrons, with four-momenta p_1, p_2 , are scattered through polar angles θ_1, θ_2 with energies E_1, E_2 respectively. The probe and target photon have four-momenta $k_1 = (x_1 E_{beam}, \vec{k}_1)$ and $k_2 = (x_2 E_{beam}, \vec{k}_2)$ and virtualities $Q^2 = -k_1^2$ and $t^2 = -k_2^2$, where:

$$Q^2 \simeq 2E_{beam}E_1(1 - \cos\theta_1).$$

The Bjorken scaling variables x and y are defined as:

$$x = \frac{Q^2}{2k_1 \cdot k_2} = \frac{Q^2}{Q^2 + t^2 + W_{\gamma\gamma}^2} \quad \text{and} \quad y = \frac{k_2 \cdot k_1}{k_2 \cdot p_1} \simeq 1 - \frac{E_1}{E_{beam}} \cos^2 \frac{\theta_1}{2} \simeq x_1,$$

where the mass squared of the produced lepton pair is $M_{ll}^2 = W_{\gamma\gamma}^2 = (k_1 + k_2)^2$. The cross section for deep-inelastic electron scattering on a photon target is the sum of the contributions of transverse (T) and longitudinal (L) photons. The differential cross section is written as [6]:

$$\frac{d^3\sigma}{dx dQ^2 dx_2} = \frac{4\pi\alpha^2}{Q^4} \frac{1}{x} \frac{dn(x_2)}{dx_2} \left\{ (1 - y + \frac{y^2}{2}) F_2^\gamma(x, Q^2) + \frac{y^2}{2} F_L^\gamma(x, Q^2) \right\}, \quad (1)$$

where the flux of target photons is given by:

$$\frac{dn(x_2)}{dx_2} = \frac{\alpha}{\pi x_2} \left\{ [1 + (1 - x_2)^2] \ln \left(\frac{2E_{beam}(1 - x_2)}{m_e x_2} \sin \frac{\theta_2^{max}}{2} \right) - 1 + x_2 \right\}. \quad (2)$$

The polar angle θ_2 of the unobserved electron is restricted to be smaller than θ_2^{max} which is also the minimum polar angle for the tagged electron, θ_1^{min} . The photon structure functions F_T^γ and F_L^γ are proportional to the cross sections σ_{ij} for transversely and longitudinally polarised virtual photons

$$F_T^\gamma \propto \sigma_{TT}, \quad F_L^\gamma \propto \sigma_{TL} \quad \text{and} \quad F_2^\gamma = 2xF_T^\gamma + F_L^\gamma.$$

The first index of the cross sections refers to the target photon, the second to the probe photon. In the present analysis, y^2 is small, on average $< 4.5 \cdot 10^{-4}$; therefore the measurement of the differential cross section is sensitive only to F_2^γ . Neglecting terms of order m_l^2/Q^2 , the QED prediction for the photon structure function F_2^γ is [6]:

$$F_2^\gamma = \frac{\alpha}{\pi} x \left\{ [x^2 + (1-x)^2] \ln \frac{W_{\gamma\gamma}^2}{m_l^2 + t^2 x(1-x)} - 1 + 8x(1-x) + \frac{t^2 x(1-x)}{m_l^2 + t^2 x(1-x)} \right\} \quad (3)$$

The scattering amplitude of longitudinally polarised photons is observed by measuring angular correlations in the $\gamma\gamma$ centre-of-mass system [6–9]. The polar angle θ^* and the azimuthal angle χ of the μ^- are defined as shown in Figure 1, where the target photon direction is assumed to be parallel to the beam axis. The azimuthal angle χ is defined as the angle between the scattering plane of the tagged electron and the plane defined by the μ^- direction and the $\gamma\gamma$ axis. The decomposition of the cross section into contributions from the different photon helicity amplitudes leads to a formula with 13 terms, each having a different azimuthal dependence. In the single tag configuration, after neglecting the longitudinal component of the target photon, only three terms remain in the cross section formula:

$$\frac{d^4\sigma}{dx dy dz d\chi} = \frac{2\pi\alpha^2}{Q^2} \frac{1 + (1-y)^2}{xy} [A_1(x, z) + A_2(x, z) \cdot \cos \chi + A_3(x) \cdot \cos 2\chi], \quad (4)$$

where $z = \cos \theta^*$. The coefficients A_1, A_2 and A_3 are related to three differential structure functions $\tilde{F}_2^\gamma, \tilde{F}_A^\gamma$ and \tilde{F}_B^γ [8]:

$$\begin{aligned} A_1 &= \tilde{F}_2^\gamma(x, z) = 2x\tilde{F}_T^\gamma(x, z) + \tilde{F}_L^\gamma(x), \\ A_2 &= -\tilde{F}_A^\gamma(x, z), \\ A_3 &= \frac{1}{2}\tilde{F}_B^\gamma(x). \end{aligned} \quad (5)$$

The sum of the amplitudes squared of the helicity states is given by A_1 , while A_2 and A_3 are interference terms leading to $\cos \chi$ and $\cos 2\chi$ modulations [7]. The coefficients A_i are calculable in QED. Setting $1-y \simeq 1$ in the $\gamma\gamma$ luminosity functions [1] they are expressed by :

$$\begin{aligned} A_1 &= \frac{x\alpha}{\pi} \left([x^2 + (1-x)^2] \frac{1 + (\beta z)^2}{1 - (\beta z)^2} + 4x(1-x) \right), \\ A_2 &= -\frac{4\alpha}{\pi} x(1-2x) \sqrt{x(1-x)} \frac{z}{\sqrt{1 - (\beta z)^2}}, \\ A_3 &= \frac{2\alpha}{\pi} x^2(1-x), \end{aligned}$$

where $\beta = \sqrt{1 - 4xm_l^2/[Q^2(1-x)]}$. The structure functions F_2^γ, F_A^γ and F_B^γ are obtained by integrating \tilde{F}_i^γ over z . The coefficient A_2 is sensitive to the amplitude with two-photon helicity $\lambda = 1$, see Figure 1, whose square is the longitudinal structure function. The interference between two transverse photons is described by $A_3 \propto \tilde{F}_B^\gamma$. It must be noted that, although F_L^γ and F_B^γ are described in QED by the same function of x , and, although in the literature both are referred to as F_L^γ [9], they correspond to a different helicity structure of the two photons. Indeed, in F_B^γ the photons are purely transverse.

3 Data analysis

The data have been collected at LEP from 1991 to 1994 at the Z peak and correspond to an integrated luminosity of 93.7 pb^{-1} . A description of the L3 detector is given elsewhere [10]. The analysis described in this paper is based on the central tracker, the BGO electromagnetic (EM) and the hadron calorimeters. The luminosity monitors [11], consisting of two BGO electromagnetic calorimeters, allow electron tagging in the regions $1.4^\circ \leq \theta \leq 3.9^\circ$ and $176.1^\circ \leq \theta \leq 178.6^\circ$.

Single tag two-photon events are mainly collected by a trigger requiring an energy deposit greater than 30 GeV in the luminosity monitors and at least one track in the central tracking chamber with a transverse momentum $p_t > 0.1 \text{ GeV}$. Other triggers [10,12] may be activated by the same events and allow to measure the trigger inefficiencies. They are 1.3% for the electron channel and 2.7% for the muon channel, independent of Q^2 and x .

The tagged electron candidate is defined as a single shower energy deposit in the luminosity monitors with $E \geq 0.75E_{beam}$, within the fiducial regions $1.55^\circ \leq \theta \leq 3.67^\circ$ and $176.33^\circ \leq \theta \leq 178.45^\circ$, which excludes the innermost and outermost crystals of the detectors. Single tag events are selected by requiring that no other electron candidate with $E \geq 0.75E_{beam}$ is seen in the complete L3 detectors. Double-tag event candidates are a few per cent of the single tag sample and are efficiently rejected.

The lepton pair is selected by requiring two tracks with opposite charges, inside a polar angle region $28^\circ \leq \theta \leq 152^\circ$, with a maximum distance of closest approach from the nominal vertex, in the plane transverse to the beam direction, of 10 mm and a transverse momentum $p_t > 0.1 \text{ GeV}$.

The electrons and muons are identified by comparing the momentum measured by the tracking chamber with the energy deposit in the electromagnetic calorimeter, E_{EM} , and by using hadron calorimeter information. Electrons are identified by the following criteria:

- in the central region, $44^\circ \leq \theta \leq 136^\circ$, the ratio $R = E_{EM} \sin \theta / p_t$ must be greater than 0.8 and the energy deposit $E_{EM} \geq 0.4 \text{ GeV}$
- in the forward-backward regions, where the measurements are less accurate, R must be greater than 0.7 and $E_{EM} \geq 0.6 \text{ GeV}$.

Muons are identified by the following criteria:

- an energy deposit $E_{EM} < 0.40 \text{ GeV}$ in the electromagnetic calorimeter, where the signal of a minimum ionising particle is, on average, 0.22 GeV. More than 95% of the energy must be contained in at most 6 neighbouring BGO crystals
- an energy deposit in the hadron calorimeter, consistent with a minimum ionising particle, associated with the selected track. This requirement implies that the energy of the muon is greater than 1.7 GeV.

For both e^+e^- and $\mu^+\mu^-$ pairs, only one identified particle is required in order to cover uniformly the angular range defined by the tracks. The effective mass of the lepton pair is required to be greater than 0.5 GeV.

For the e^+e^- sample, in 76% of the events both electrons are identified. For the $\mu^+\mu^-$ sample, in 40% of the events both muons reach the hadron calorimeter and have a minimum ionising particle signature. A more detailed description of the analysis is given in Reference [13].

Two event generators [14, 15] together with a full detector simulation [16], are used to calculate the selection efficiencies. The first one [14] calculates the full set of QED diagrams to $O(\alpha^4)$, taking into account interference effects. It shows that, in the kinematical regions of this analysis, only the contribution of the multiperipheral diagrams is non-negligible. The second one [15] which is much faster and has exact calculations only for the multiperipheral diagram, is used to produce large statistics Monte Carlo samples. These generators do not simulate initial state radiation. To estimate the effect of initial state radiation another generator [17], which simulates the process $e^+e^- \rightarrow e^+e^-\mu^+\mu^-(\gamma)$, is used.

The same generators [14, 15] are also used to estimate the $e^+e^- \rightarrow e^+e^-\tau^+\tau^-$ and $e^+e^- \rightarrow e^+e^-q\bar{q}$ backgrounds. The background is 0.9% for the electron channel dominated by $\tau^+\tau^-$ production. It is 1.8% for the muon channel due to misidentified electrons (0.78%), $\tau^+\tau^-$ production (0.71%) and $q\bar{q}$ production (0.32%).

The background from radiative Z decays, where an emitted photon fakes the tagged electron, is found to be negligible, by simulating the annihilation processes with the generators KORALZ [18] and JETSET [19].

The number of selected events, for each channel, after background subtraction, is reported in Table 1 together with the Monte Carlo [14] expectations. The distributions of the polar angle and of the effective mass $W_{\gamma\gamma}$ for the electron and muon pairs are shown in Figure 2. They are in agreement with the Monte Carlo [14] expectations in shape and in absolute value.

4 Results

To calculate the differential cross sections, the data are corrected for acceptance and efficiency in bins of x and Q^2 . The differential cross sections $d\sigma/dQ^2$ are shown in Figure 3 for $1.4 \text{ GeV}^2 < Q^2 < 7.6 \text{ GeV}^2$ and $W_{\gamma\gamma} > 0.5 \text{ GeV}$, together with analytical QED predictions obtained from Equation 1.

The systematic error comes from selection procedure, trigger efficiency, background subtraction and luminosity measurements. It is 3.3% for the di-muon channel and 1.7% for the di-electron channel and is found to be independent of Q^2 and x [13].

4.1 Determination of F_2^γ

The structure function F_2^γ , as defined in Equation 1, is extracted from the differential cross section, extrapolated to the full phase space, with no cut on $W_{\gamma\gamma}$:

$$F_2^\gamma(x, Q^2) = \mathcal{W}(x, Q^2) \frac{d^2\sigma}{dx dQ^2}$$

The weight $\mathcal{W}(x, Q^2)$ is calculated analytically using Monte Carlo events, for each bin of x and Q^2 , integrating the differential weight $\widetilde{\mathcal{W}}$ over the kinematically allowed range of the scaled target photon energy x_2 :

$$\frac{1}{\widetilde{\mathcal{W}}(x, Q^2, x_2)} = K(x, Q^2, x_2) = \frac{8\pi\alpha^2}{Q^2} \frac{x_2}{x} \left\{ \left(\frac{s + Q^2}{W_{\gamma\gamma}^2 + Q^2} \right) x_2 - 1 \right\} \frac{dn(x_2)}{dx_2}, \quad (6)$$

where $dn(x_2)/dx_2$ is the target photon flux defined in Equation 2. After changing variables from Q^2, x, x_2 to Q^2, x, x_1 , for each Monte Carlo event we calculate the average value

$$\mathcal{W}(x, Q^2) = \left\langle \frac{1}{K(x, Q^2, x_1)} \right\rangle = \int_{x_1^{min}}^{x_1^{max}} \frac{dx_1}{(x_1^{max} - x_1^{min}) K(x, Q^2, x_1)}.$$

The kinematically allowed limits on x_1 are

$$x_1^{max} = \min \left\{ 1 - \frac{E_0}{E_{beam}}, 1 - \frac{Q^2}{s \sin^2(\theta_1^{max}/2)} \right\}, \quad x_1^{min} = \max \left\{ \frac{W_{\gamma\gamma}^2}{s}, 1 - \frac{Q^2}{s \sin^2(\theta_1^{max}/2)} \right\}$$

where E_0 is the minimum allowed energy of the tagged electron and $s = 4E_{beam}^2$.

The values of F_2^γ , thus obtained for the di-muon channel, are shown in Figure 4. Assuming the target photon to be real ($t^2 = 0$), the QED predictions are significantly higher than the measured values: $\chi^2/dof = 107/10$, corresponding to a probability $< 10^{-4}$. Equation 3, fitted to the data, gives a mean value for the virtuality $\langle t^2 \rangle = 0.033 \pm 0.005 \text{ GeV}^2$ with a probability of 8%. The fitted value of the virtuality is in excellent agreement with the value of $0.034 \pm 0.002 \text{ GeV}^2$ calculated by the Monte Carlo including radiative corrections [17]. Without radiative corrections the expected mean virtuality of the target photon is $\langle t^2 \rangle = 0.024 \pm 0.003$, two standard deviations below the measurement. This measurement demonstrates that the correction due to the target photon virtuality cannot be neglected in studies of hadronic structure functions of the photon. The theoretical parametrisations of parton density functions must include also the dependence of the target photon virtuality, as underlined in [20].

4.2 Azimuthal Correlations and Determination of F_A^γ and F_B^γ

In Figure 5 the generated distribution of $z = \cos \theta^*$ is presented. It increases rapidly towards $z = \pm 1$. Also plotted in Figure 5 is the selection efficiency, i.e. the ratio of selected events, after the full simulation and the analysis cuts, over the generated events. The selection efficiency drops to zero at $z = \pm 1$, due to the limited acceptance at small polar angle. The events in the central region, where the acceptance is high and uniform, are the most sensitive to the interference of the transverse and longitudinal photon amplitudes. The azimuthal correlation measurement is therefore restricted to $|z| \leq 0.7$. The measured angular distributions are well reproduced by the Monte Carlo simulation [13]. The data are corrected for acceptance and efficiency over a two-dimensional grid in the variables z and χ . Several correction methods are used to extract the azimuthal distributions, taking into account detector acceptance and resolution effects: a bin-by-bin correction using the ratio of reconstructed events over generated events and two unfolding algorithms [21, 22]. The unfolding of Reference [21] is used in the analysis. The χ distributions are fitted using a function of the form

$$\frac{dN}{d\chi} = C[1 + R_\chi \cos \chi + R_{2\chi} \cos 2\chi] \quad (7)$$

with R_χ , $R_{2\chi}$ and C let as free parameters. From Equations 4 and 5, it follows that $C \propto F_2^\gamma$, $R_\chi \propto F_A^\gamma/F_2^\gamma$ and $R_{2\chi} \propto F_B^\gamma/F_2^\gamma$. The x range is subdivided in four intervals. The coefficient $R_{2\chi}$ is symmetric in z and is determined by a fit over the range $-0.7 < z < 0.7$, where R_χ vanishes. The fit result, superimposed to the data, is shown in Figure 6. Since F_A^γ is antisymmetric in z , the x dependence of R_χ is studied in the ranges $-0.7 < z < 0$ and $0 < z < 0.7$. In Figure 7 the sample with $z < 0$ is added to the sample with $z > 0$, using the transformation $\chi \rightarrow \pi - \chi$. The fit results of R_χ and $R_{2\chi}$ are given in Table 2 with statistical and systematic errors.

Several sources of systematic errors on the measurement of R_χ and $R_{2\chi}$ are taken into account. The effects of detector resolution on the variables Q^2 , x , z and χ are tested by Monte Carlo simulations, varying each variable in turn, according to its resolution. This leads to a systematic error of 8% on R_χ and $R_{2\chi}$. The muon momentum resolution produces a systematic uncertainty of 12%. By comparing predictions of the generators [14] and [17], a systematic

error of 4% is assigned to the effect of radiative corrections. The effects of cuts on z and x contribute less than 3%. From the average deviation between the results obtained with the three different unfolding methods used to correct the data, systematic errors of 1% on R_χ and 13% on $R_{2\chi}$ are estimated.

To determine F_A^γ and F_B^γ , the measurement is extrapolated to the full z range. A set of correction factors C_{R_χ} and $C_{R_{2\chi}}$ are calculated by numerical integration and reported in Table 2. The structure functions F_A^γ and F_B^γ are extracted as:

$$F_A^\gamma = \frac{1}{2}C_{R_\chi}R_\chi F_2^\gamma, \quad F_B^\gamma = 2C_{R_{2\chi}}R_{2\chi}F_2^\gamma. \quad (8)$$

Their values are given in Table 2 and shown in Figure 8 together with the QED expectations. Good agreement is found in shape and absolute value. These results are the first measurements of the dependence of the structure functions F_A^γ and F_B^γ on the scaling variable x . The interference term of the longitudinal photon present in the structure function F_A^γ is small, as expected, but measurable.

5 Conclusions

We have measured the differential cross sections of the single tag two-photon reaction $e^+e^- \rightarrow e^+e^-e^+e^-$ and $e^+e^- \rightarrow e^+e^-\mu^+\mu^-$ at $\sqrt{s} \simeq 91$ GeV, using data collected by the L3 detector at LEP during the years 1991 to 1994. The data are in good agreement with QED predictions.

In the channel $e^+e^- \rightarrow e^+e^-\mu^+\mu^-$, the leptonic structure function F_2^γ is extracted from the differential cross section $d^2\sigma/dxdQ^2$ in the Q^2 range $1.4 \text{ GeV}^2 < Q^2 < 7.6 \text{ GeV}^2$.

By fitting the data, the mean value of the target photon virtuality is found to be $\langle t^2 \rangle = 0.033 \pm 0.005 \text{ GeV}^2$, in good agreement with QED predictions. Neglecting initial state radiative corrections the theory expectations are two standard deviations below the measurement.

The first measurement of the F_A^γ and F_B^γ leptonic structure functions is obtained by studying the azimuthal angle distribution of the μ^- in the $\gamma\gamma$ centre-of-mass system. Both structure functions originate from interference terms of the scattering amplitudes. The x dependence of the interference terms, as predicted by QED, is indeed observed. This measurement establishes the presence of a longitudinal photon component in the single tag two-photon reaction.

6 Acknowledgements

We express our gratitude to the CERN accelerator divisions for the excellent performance of the LEP machine. We acknowledge with appreciation the effort of all engineers, technicians and support staff who have participated in the construction and maintenance of this experiment. We wish to thank G. d'Agostini, F.A. Berends and G.A. Schuler for useful discussions.

The L3 Collaboration:

M. Acciarri,²⁷ O. Adriani,¹⁶ M. Aguilar-Benitez,²⁶ S. Ahlen,¹¹ J. Alcaraz,²⁶ G. Alemani,²² J. Allaby,¹⁷ A. Aloisio,²⁹
 M.G. Alvigi,²⁹ G. Ambrosi,¹⁹ H. Anderhub,⁴⁸ V.P. Andreev,³⁷ T. Angelescu,¹³ F. Anselmo,⁹ A. Arefiev,²⁸ T. Azemoon,³
 T. Aziz,¹⁰ P. Bagnaia,³⁶ L. Baksay,⁴³ R.C. Ball,³ S. Banerjee,¹⁰ Sw. Banerjee,¹⁰ K. Banicz,⁴⁵ A. Barczyk,^{48,46} R. Barillère,¹⁷
 L. Barone,³⁶ P. Bartalini,²² A. Baschirotto,²⁷ M. Basile,⁹ R. Battiston,³³ A. Bay,²² F. Becattini,¹⁶ U. Becker,¹⁵ F. Behner,⁴⁸
 J. Berdugo,²⁶ P. Berges,¹⁵ B. Bertucci,³³ B.L. Betev,⁴⁸ S. Bhattacharya,¹⁰ M. Biasini,³³ A. Biland,⁴⁸ G.M. Bilei,³³
 J.J. Blaising,⁴ S.C. Blyth,³⁴ G.J. Bobbink,² R. Bock,¹ A. Böhm,¹ L. Boldizar,¹⁴ B. Borgia,^{17,36} D. Bourilkov,⁴⁸
 M. Bourquin,¹⁹ D. Boutigny,⁴ S. Braccini,¹⁹ J.G. Branson,³⁹ V. Brigljevic,⁴⁸ I.C. Brock,³⁴ A. Buffini,¹⁶ A. Buijs,⁴⁴
 J.D. Burger,¹⁵ W.J. Burger,³³ J. Busenitz,⁴³ X.D. Cai,¹⁵ M. Campanelli,⁴⁸ M. Capell,¹⁵ G. Cara Romeo,⁹ G. Carlino,²⁹
 A.M. Cartacci,¹⁶ J. Casaus,²⁶ G. Castellini,¹⁶ F. Cavallari,³⁶ N. Cavallo,²⁹ C. Cecchi,¹⁹ M. Cerrada,²⁶ F. Cesaroni,²³
 M. Chamizo,²⁶ Y.H. Chang,⁵⁰ U.K. Chaturvedi,¹⁸ S.V. Chekanov,³¹ M. Chemarin,²⁵ A. Chen,⁵⁰ G. Chen,⁷ G.M. Chen,⁷
 H.F. Chen,²⁰ H.S. Chen,⁷ M. Chen,¹⁵ G. Chiefari,²⁹ C.Y. Chien,⁵ L. Cifarelli,³⁸ F. Cindolo,⁹ C. Civinini,¹⁶ I. Clare,¹⁵
 R. Clare,¹⁵ G. Coignet,⁴ A.P. Colijn,² N. Colino,²⁶ S. Costantini,⁸ F. Cotorobai,¹³ B. de la Cruz,²⁶ A. Csilling,¹⁴ T.S. Dai,¹⁵
 R.D' Alessandro,¹⁶ R. de Asmundis,²⁹ A. Degre,⁴ K. Deiters,⁴⁶ P. Denes,³⁵ F. DeNotaristefani,³⁶ M. Diemoz,³⁶
 D. van Dierendonck,² F. Di Lodovico,⁴⁸ C. Dionisi,^{17,36} M. Dittmar,⁴⁸ A. Dominguez,³⁹ A. Doria,²⁹ M.T. Dova,^{18,‡}
 E. Drago,²⁹ D. Duchesneau,⁴ P. Duinker,² I. Duran,⁴⁰ S. Easo,³³ H. El Mamouni,²⁵ A. Engler,³⁴ F.J. Eppling,¹⁵ F.C. Erne,²
 J.P. Ernenwein,²⁵ P. Extermann,¹⁹ M. Fabre,⁴⁶ R. Faccini,³⁶ M.A. Falagan,²⁶ S. Falciano,³⁶ A. Favara,¹⁶ J. Fay,²⁵ O. Fedin,³⁷
 M. Felcini,⁴⁸ T. Ferguson,³⁴ F. Ferroni,³⁶ H. Fesefeldt,¹ E. Fiandrini,³³ J.H. Field,¹⁹ F. Filthaut,¹⁷ P.H. Fisher,¹⁵ I. Fisk,³⁹
 G. Forconi,¹⁵ L. Fredj,¹⁹ K. Freudenreich,⁴⁸ C. Furetta,²⁷ Yu. Galaktionov,^{28,15} S.N. Ganguli,¹⁰ P. Garcia-Abia,⁶
 M. Gataullin,³² S.S. Gau,¹² S. Gentile,³⁶ J. Gerald,⁵ N. Gheordanescu,¹³ S. Giagu,³⁶ S. Goldfarb,²² J. Goldstein,¹¹
 Z.F. Gong,²⁰ A. Gougas,⁵ G. Gratta,³² M.W. Gruenewald,⁸ R. van Gulik,² V.K. Gupta,³⁵ A. Gurtu,¹⁰ L.J. Gutay,⁴⁵
 D. Haas,⁶ B. Hartmann,¹ A. Hasan,³⁰ D. Hatzifotiadou,⁹ T. Hebbeker,⁸ A. Herve,¹⁷ P. Hidas,¹⁴ J. Hirschfelder,³⁴
 W.C. van Hoek,³¹ H. Hofer,⁴⁸ H. Hoorani,³⁴ S.R. Hou,⁵⁰ G. Hu,⁵ I. Iashvili,⁴⁷ B.N. Jin,⁷ L.W. Jones,³ P. de Jong,¹⁷
 L. Josa-Mutuberria,²⁶ A. Kasser,²² R.A. Khan,¹⁸ D. Kamrad,⁴⁷ J.S. Kapustinsky,²⁴ Y. Karyotakis,⁴ M. Kaur,^{18,◇}
 M.N. Kienzle-Focacci,¹⁹ D. Kim,³⁶ D.H. Kim,⁴² J.K. Kim,⁴² S.C. Kim,⁴² W.W. Kinnison,²⁴ A. Kirkby,³² D. Kirkby,³²
 J. Kirkby,¹⁷ D. Kiss,¹⁴ W. Kittel,³¹ A. Klimentov,^{15,28} A.C. König,³¹ A. Kopp,⁴⁷ I. Korolko,²⁸ V. Koutsenko,^{15,28}
 R.W. Kraemer,³⁴ W. Krenz,¹ A. Kunin,^{15,28} P. Lacentre,^{47,‡,‡} P. Ladron de Guevara,²⁶ G. Landi,¹⁶ C. Lapoint,¹⁵
 K. Lassila-Perini,⁴⁸ P. Laurikainen,²¹ A. Lavorato,³⁸ M. Lebeau,¹⁷ A. Lebedev,¹⁵ P. Lebrun,²⁵ P. Lecomte,⁴⁸ P. Lecoq,¹⁷
 P. Le Coultre,⁴⁸ H.J. Lee,⁸ C. Leggett,³ J.M. Le Goff,¹⁷ R. Leiste,⁴⁷ E. Leonardi,³⁶ P. Levchenko,³⁷ C. Li,²⁰ C.H. Lin,⁵⁰
 W.T. Lin,⁵⁰ F.L. Linde,^{2,17} L. Lista,²⁹ Z.A. Liu,⁷ W. Lohmann,⁴⁷ E. Longo,³⁶ W. Lu,³² Y.S. Lu,⁷ K. Lübelmeyer,¹
 C. Luci,^{17,36} D. Luckey,¹⁵ L. Luminari,³⁶ W. Luster mann,⁴⁸ W.G. Ma,²⁰ M. Maity,¹⁰ G. Majumder,¹⁰ L. Malgeri,¹⁷
 A. Malinin,²⁸ C. Mañá,²⁶ D. Mangeol,³¹ P. Marchesini,⁴⁸ G. Marian,^{43,§} A. Marin,¹¹ J.P. Martin,²⁵ F. Marzano,³⁶
 G.G.G. Massaro,² K. Mazumdar,¹⁰ S. Mele,¹⁷ L. Merola,²⁹ M. Meschini,¹⁶ W.J. Metzger,³¹ M. von der Mey,¹ Y. Mi,²²
 D. Migani,⁹ A. Mihul,³ A.J.W. van Mil,³¹ H. Milcent,¹⁷ G. Mirabelli,³⁶ J. Mnich,¹⁷ P. Molnar,⁸ B. Monteleoni,¹⁶ R. Moore,³
 T. Moulík,¹⁰ R. Mount,³² F. Muheim,¹⁹ A.J.M. Muijs,² S. Nahn,¹⁵ M. Napolitano,²⁹ F. Nessi-Tedaldi,⁴⁸ H. Newman,³²
 T. Niessen,¹ A. Nippe,²² A. Nisati,³⁶ H. Nowak,⁴⁷ Y.D. Oh,⁴² G. Organtini,³⁶ R. Ostonen,²¹ S. Palit,¹² C. Palomares,²⁶
 D. Pandoulas,¹ S. Paoletti,³⁶ P. Paolucci,²⁹ H.K. Park,³⁴ I.H. Park,⁴² G. Pascale,³⁶ G. Passaleva,¹⁷ S. Patricelli,²⁹ T. Paul,¹²
 M. Pauluzzi,³³ C. Paus,¹⁷ F. Pauss,⁴⁸ D. Peach,¹⁷ Y.J. Pei,¹ S. Pensotti,²⁷ D. Perret-Gallix,⁴ B. Petersen,³¹ S. Petrak,⁸
 A. Pevsner,⁵ D. Piccolo,²⁹ M. Pieri,¹⁶ P.A. Piroué,³⁵ E. Pistolesi,²⁷ V. Plyaskin,²⁸ M. Pohl,⁴⁸ V. Pojidaev,^{28,16} H. Postema,¹⁵
 J. Pothier,¹⁷ N. Produit,¹⁹ D. Prokofiev,³⁷ J. Quartieri,³⁸ G. Rahal-Callot,⁴⁸ N. Raja,¹⁰ P.G. Rancoita,²⁷ M. Rattaggi,²⁷
 G. Raven,³⁹ P. Razis,³⁰ D. Ren,⁴⁸ M. Rescigno,³⁶ S. Reucroft,¹² T. van Rhee,⁴⁴ S. Riemann,⁴⁷ K. Riles,³ O. Rind,³
 A. Robohm,⁴⁸ J. Rodin,⁴³ B.P. Roe,³ L. Romero,²⁶ S. Rosier-Lees,⁴ Ph. Rosset,²² S. Roth,¹ J.A. Rubio,¹⁷ D. Ruschmeier,⁸
 H. Rykaczewski,⁴⁸ J. Salicio,¹⁷ E. Sanchez,²⁶ M.P. Sanders,³¹ M.E. Sarakinos,²¹ G. Sauvage,⁴ C. Schäfer,¹ V. Schegelsky,³⁷
 S. Schmidt-Kaerst,¹ D. Schmitz,¹ M. Schneegans,⁴ N. Scholz,⁴⁸ H. Schopper,⁴⁹ D.J. Schotanus,³¹ J. Schwenke,¹
 G. Schwering,¹ C. Sciacca,²⁹ D. Sciarino,¹⁹ L. Servoli,³³ S. Shevchenko,³² N. Shivarov,⁴¹ V. Shoutko,²⁸ J. Shukla,²⁴
 E. Shumilov,²⁸ A. Shvorob,³² T. Siedenburtg,¹ D. Son,⁴² V. Soulimov,²⁹ B. Smith,¹⁵ P. Spillantini,¹⁶ M. Steuer,¹⁵
 D.P. Stickland,³⁵ H. Stone,³⁵ B. Stoyanov,⁴¹ A. Straessner,¹ K. Sudhakar,¹⁰ G. Sultanov,¹⁸ L.Z. Sun,²⁰ G.F. Susinno,¹⁹
 H. Suter,⁴⁸ J.D. Swain,¹⁸ X.W. Tang,⁷ L. Tauscher,⁶ L. Taylor,¹² Samuel C.C. Ting,¹⁵ S.M. Ting,¹⁵ S.C. Tonwar,¹⁰ J. Tóth,¹⁴
 C. Tully,³⁵ K.L. Tung,⁷ Y. Uchida,¹⁵ J. Ulbricht,⁴⁸ E. Valente,³⁶ G. Vesztegombi,¹⁴ I. Vetlitsky,²⁸ G. Viertel,⁴⁸
 M. Vivargent,⁴ S. Vlachos,⁶ H. Vogel,³⁴ H. Vogt,⁴⁷ I. Vorobiev,^{17,28} A.A. Vorobyov,³⁷ A. Vorvolakos,³⁰ M. Wadhwa,⁶
 W. Wallraff,¹ J.C. Wang,¹⁵ X.L. Wang,²⁰ Z.M. Wang,²⁰ A. Weber,¹ S.X. Wu,¹⁵ S. Wynhoff,¹ J. Xu,¹¹ Z.Z. Xu,²⁰ B.Z. Yang,²⁰
 C.G. Yang,⁷ H.J. Yang,⁷ M. Yang,⁷ J.B. Ye,²⁰ S.C. Yeh,⁵¹ J.M. You,³⁴ An. Zalite,³⁷ Yu. Zalite,³⁷ P. Zemp,⁴⁸ Y. Zeng,¹
 Z.P. Zhang,²⁰ B. Zhou,¹¹ Y. Zhou,³ G.Y. Zhu,⁷ R.Y. Zhu,³² A. Zichichi,^{9,17,18} F. Ziegler,⁴⁷ G. Zilizi.^{43,§}

- 1 I. Physikalisches Institut, RWTH, D-52056 Aachen, FRG[§]
 - III. Physikalisches Institut, RWTH, D-52056 Aachen, FRG[§]
 - 2 National Institute for High Energy Physics, NIKHEF, and University of Amsterdam, NL-1009 DB Amsterdam, The Netherlands
 - 3 University of Michigan, Ann Arbor, MI 48109, USA
 - 4 Laboratoire d'Annecy-le-Vieux de Physique des Particules, LAPP, IN2P3-CNRS, BP 110, F-74941 Annecy-le-Vieux CEDEX, France
 - 5 Johns Hopkins University, Baltimore, MD 21218, USA
 - 6 Institute of Physics, University of Basel, CH-4056 Basel, Switzerland
 - 7 Institute of High Energy Physics, IHEP, 100039 Beijing, China[△]
 - 8 Humboldt University, D-10099 Berlin, FRG[§]
 - 9 University of Bologna and INFN-Sezione di Bologna, I-40126 Bologna, Italy
 - 10 Tata Institute of Fundamental Research, Bombay 400 005, India
 - 11 Boston University, Boston, MA 02215, USA
 - 12 Northeastern University, Boston, MA 02115, USA
 - 13 Institute of Atomic Physics and University of Bucharest, R-76900 Bucharest, Romania
 - 14 Central Research Institute for Physics of the Hungarian Academy of Sciences, H-1525 Budapest 114, Hungary[‡]
 - 15 Massachusetts Institute of Technology, Cambridge, MA 02139, USA
 - 16 INFN Sezione di Firenze and University of Florence, I-50125 Florence, Italy
 - 17 European Laboratory for Particle Physics, CERN, CH-1211 Geneva 23, Switzerland
 - 18 World Laboratory, FBLJA Project, CH-1211 Geneva 23, Switzerland
 - 19 University of Geneva, CH-1211 Geneva 4, Switzerland
 - 20 Chinese University of Science and Technology, USTC, Hefei, Anhui 230 029, China[△]
 - 21 SEFT, Research Institute for High Energy Physics, P.O. Box 9, SF-00014 Helsinki, Finland
 - 22 University of Lausanne, CH-1015 Lausanne, Switzerland
 - 23 INFN-Sezione di Lecce and Università Degli Studi di Lecce, I-73100 Lecce, Italy
 - 24 Los Alamos National Laboratory, Los Alamos, NM 87544, USA
 - 25 Institut de Physique Nucléaire de Lyon, IN2P3-CNRS, Université Claude Bernard, F-69622 Villeurbanne, France
 - 26 Centro de Investigaciones Energéticas, Medioambientales y Tecnológicas, CIEMAT, E-28040 Madrid, Spain^b
 - 27 INFN-Sezione di Milano, I-20133 Milan, Italy
 - 28 Institute of Theoretical and Experimental Physics, ITEP, Moscow, Russia
 - 29 INFN-Sezione di Napoli and University of Naples, I-80125 Naples, Italy
 - 30 Department of Natural Sciences, University of Cyprus, Nicosia, Cyprus
 - 31 University of Nijmegen and NIKHEF, NL-6525 ED Nijmegen, The Netherlands
 - 32 California Institute of Technology, Pasadena, CA 91125, USA
 - 33 INFN-Sezione di Perugia and Università Degli Studi di Perugia, I-06100 Perugia, Italy
 - 34 Carnegie Mellon University, Pittsburgh, PA 15213, USA
 - 35 Princeton University, Princeton, NJ 08544, USA
 - 36 INFN-Sezione di Roma and University of Rome, "La Sapienza", I-00185 Rome, Italy
 - 37 Nuclear Physics Institute, St. Petersburg, Russia
 - 38 University and INFN, Salerno, I-84100 Salerno, Italy
 - 39 University of California, San Diego, CA 92093, USA
 - 40 Dept. de Física de Partículas Elementales, Univ. de Santiago, E-15706 Santiago de Compostela, Spain
 - 41 Bulgarian Academy of Sciences, Central Lab. of Mechatronics and Instrumentation, BU-1113 Sofia, Bulgaria
 - 42 Center for High Energy Physics, Adv. Inst. of Sciences and Technology, 305-701 Taejeon, Republic of Korea
 - 43 University of Alabama, Tuscaloosa, AL 35486, USA
 - 44 Utrecht University and NIKHEF, NL-3584 CB Utrecht, The Netherlands
 - 45 Purdue University, West Lafayette, IN 47907, USA
 - 46 Paul Scherrer Institut, PSI, CH-5232 Villigen, Switzerland
 - 47 DESY-Institut für Hochenergiephysik, D-15738 Zeuthen, FRG
 - 48 Eidgenössische Technische Hochschule, ETH Zürich, CH-8093 Zürich, Switzerland
 - 49 University of Hamburg, D-22761 Hamburg, FRG
 - 50 National Central University, Chung-Li, Taiwan, China
 - 51 Department of Physics, National Tsing Hua University, Taiwan, China
- [§] Supported by the German Bundesministerium für Bildung, Wissenschaft, Forschung und Technologie
[‡] Supported by the Hungarian OTKA fund under contract numbers T019181, F023259 and T024011.
[§] Also supported by the Hungarian OTKA fund under contract numbers T22238 and T026178.
^b Supported also by the Comisión Interministerial de Ciencia y Tecnología.
[#] Also supported by CONICET and Universidad Nacional de La Plata, CC 67, 1900 La Plata, Argentina.
[‡] Supported by Deutscher Akademischer Austauschdienst.
[◇] Also supported by Panjab University, Chandigarh-160014, India.
[△] Supported by the National Natural Science Foundation of China.

References

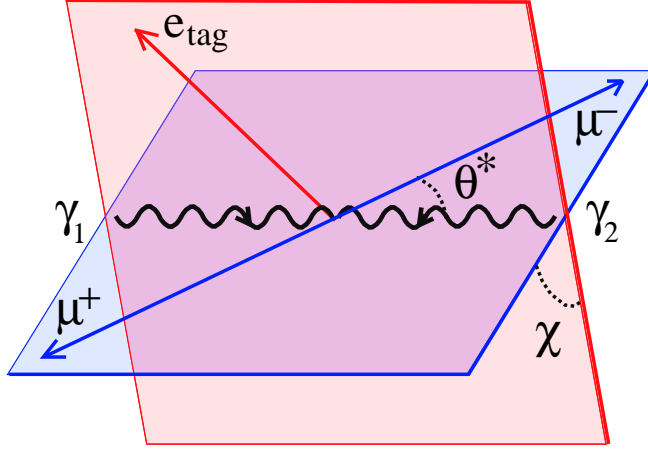
- [1] V.M. Budnev, I.F. Ginzburg, G.V. Meledin and V.G. Serbo, Phys.Rep. **C 15** (1974) 181.
- [2] L3 Collaboration, M. Acciarri *et al.*, Phys. Lett. **B 407** (1997) 341.
- [3] OPAL Collaboration, K. Ackers *et al.*, Z. Phys. **C 60** (1993) 593.
- [4] DELPHI Collaboration, P. Abreu *et al.*, Z. Phys. **C 96** (1994) 199.
- [5] OPAL Collaboration, K. Ackerstaff *et al.*, Z. Phys. **C 74** (1997) 49.
- [6] CELLO Collaboration, H.J. Behrend *et al.*, Phys. Lett. **B 126** (1983) 384.
- [7] P. Kessler, Proceedings of Photon '95, Sheffield U.K. 8-13 April 1995. eds. D.J. Miller, S.L. Cartwright and V. Khoze, World Scientific, Singapore, 281 (1995).
- [8] J.H. Field, Proceedings of Photon '95, Sheffield U.K. 8-13 April 1995. eds D.J. Miller, S.L. Cartwright and V. Khoze, World Scientific, Singapore, 485 (1995).
- [9] C. Peterson, P. Zerwas and T.F. Walsh, Nucl. Phys. **B 229** (1983) 301.
Note that in Equations (21) a factor $\frac{1}{2}$ is missing in the first equation, a factor x in the third one.
- [10] L3 Collaboration, B. Adeva *et al.*, Nucl. Inst. Meth. **A 289** (1990) 35.
- [11] L3 Collaboration, B.Adeva *et al.*, Nucl. Inst. Meth. **A 381** (1996) 236.
- [12] R. Bizzarri *et al.*, Nucl. Inst. Meth. **A 317** (1992) 463.
- [13] G. Susinno, PhD thesis 2961, Université de Genève, Switzerland, 1997.
- [14] F.A. Berends, P.H. Daverfeldt and R. Kleiss, Nucl. Phys. **B 253** (1985) 441; Comp. Phys. Comm. **40** (1986) 285.
- [15] J.Vermaseren, Nucl. Phys. **B 229** (1983) 347.
- [16] R.Brun *et al.*, " GEANT 3", CERN DD/EE/84-1 (Revised), September 1987.
- [17] F.A. Berends, P.H. Daverfeldt and R. Kleiss, Nucl. Phys. **B 253** (1985) 421; Comp. Phys. Comm. **40** (1986) 271.
- [18] KORALZ version 4.0 is used.
S. Jadach, B.F.L. Ward and Z. Was, Comp. Phys. Comm. **79** (1994) 503.
- [19] PYTHIA version 5.7 is used.
T. Sjöstrand, Comp. Phys. Comm. **82** (1994) 74.
- [20] G. Schuler and T. Sjöstrand, Phys. Lett. **B 376** (1996) 193.
- [21] G. D'Agostini, Nucl. Inst. Meth. **A 362** (1995) 487.
- [22] A. Höcker and V. Kertvelishvili, Nucl. Inst. Meth. **A 372** (1996) 469.

Process	Observed Events	Expected Events	Ratio
$e^+e^-\mu^+\mu^-$	7152 ± 85	7119 ± 42	1.005 ± 0.013
$e^+e^-e^+e^-$	3802 ± 62	3842 ± 47	0.990 ± 0.020

Table 1: Number of selected events, after background subtraction, compared to the expectations of [14].

Δx	Δz	R_χ	C_{R_χ}
0 - 0.25	0 - 0.7	$0.30 \pm 0.06 \pm 0.06$	0.6118
0.25 - 0.5	0 - 0.7	$0.10 \pm 0.07 \pm 0.05$	1.0185
0.50 - 0.75	0 - 0.7	$-0.21 \pm 0.09 \pm 0.04$	1.1368
0.75 - 1	0 - 0.7	$-0.20 \pm 0.07 \pm 0.05$	1.2089
0 - 0.25	-0.7 - 0	$-0.22 \pm 0.07 \pm 0.05$	0.6118
0.25 - 0.5	-0.7 - 0	$-0.07 \pm 0.07 \pm 0.06$	1.0185
0.50 - 0.75	-0.7 - 0	$0.16 \pm 0.09 \pm 0.06$	1.1368
0.75 - 1	-0.7 - 0	$0.19 \pm 0.08 \pm 0.08$	1.2089
Δx	Δz	$R_{2\chi}$	$C_{R_{2\chi}}$
0 - 0.25	-0.7 - 0.7	$0.24 \pm 0.06 \pm 0.06$	0.1933
0.25 - 0.5	-0.7 - 0.7	$0.35 \pm 0.06 \pm 0.12$	0.3184
0.50 - 0.75	-0.7 - 0.7	$0.38 \pm 0.07 \pm 0.13$	0.3715
0.75 - 1	-0.7 - 0.7	$0.16 \pm 0.05 \pm 0.08$	0.3812
Δx	F_2^γ	F_A^γ	F_B^γ
0 - 0.25	0.090 ± 0.008	-0.007 ± 0.012	0.008 ± 0.010
0.25 - 0.5	0.405 ± 0.016	-0.018 ± 0.016	0.090 ± 0.021
0.50 - 0.75	0.597 ± 0.020	0.063 ± 0.026	0.168 ± 0.040
0.75 - 1	0.731 ± 0.032	0.087 ± 0.031	0.089 ± 0.045

Table 2: The parameters R_χ and $R_{2\chi}$, obtained by a fit of the function of Equation 7 to the azimuthal angle, χ , distributions, are given for different x and z ranges. The first error is statistical and the second is systematic. The correction factors C_{R_χ} and $C_{R_{2\chi}}$, used to extrapolate R_χ and $R_{2\chi}$ to the full z range, are also given. In the last four rows, F_2^γ , F_A^γ and F_B^γ are given for the full z range, with the statistical and systematic errors added in quadrature.



$$A_1 : \left| \begin{array}{c} \rightarrow \\ \leftarrow \end{array} \right|^2 + \left| \begin{array}{c} \rightarrow \\ \leftarrow \end{array} \right|^2 + \left| \begin{array}{c} \circ \\ \leftarrow \end{array} \right|^2$$

$$A_2 : 2\text{Re}\left\{ \left(\begin{array}{c} \circ \\ \leftarrow \end{array} \right) \otimes \left(\begin{array}{c} \rightarrow \\ \leftarrow \end{array} \right) \right\} + \\ + 2\text{Re}\left\{ \left(\begin{array}{c} \circ \\ \leftarrow \end{array} \right) \otimes \left(\begin{array}{c} \rightarrow \\ \leftarrow \end{array} \right) \right\}$$

$$A_3 : 2\text{Re}\left\{ \left(\begin{array}{c} \rightarrow \\ \leftarrow \end{array} \right) \otimes \left(\begin{array}{c} \rightarrow \\ \leftarrow \end{array} \right) \right\}$$

Figure 1: Definition of the angles θ^* and χ in the $\gamma\gamma$ centre-of-mass frame. For a single tag configuration, the target photon is almost real and, in good approximation, purely transverse. There are only three possible independent helicity amplitudes. The relation between the coefficients A_i and the photon helicity states are schematically shown. A_1 is the quadratic sum of the total photon helicity $\lambda = 0, 2$ and 1 while A_2 and A_3 are interference terms. Target photons are represented on the right and probe photons on the left. The longitudinal component of the probe photon can be obtained from a measurement of A_2 .

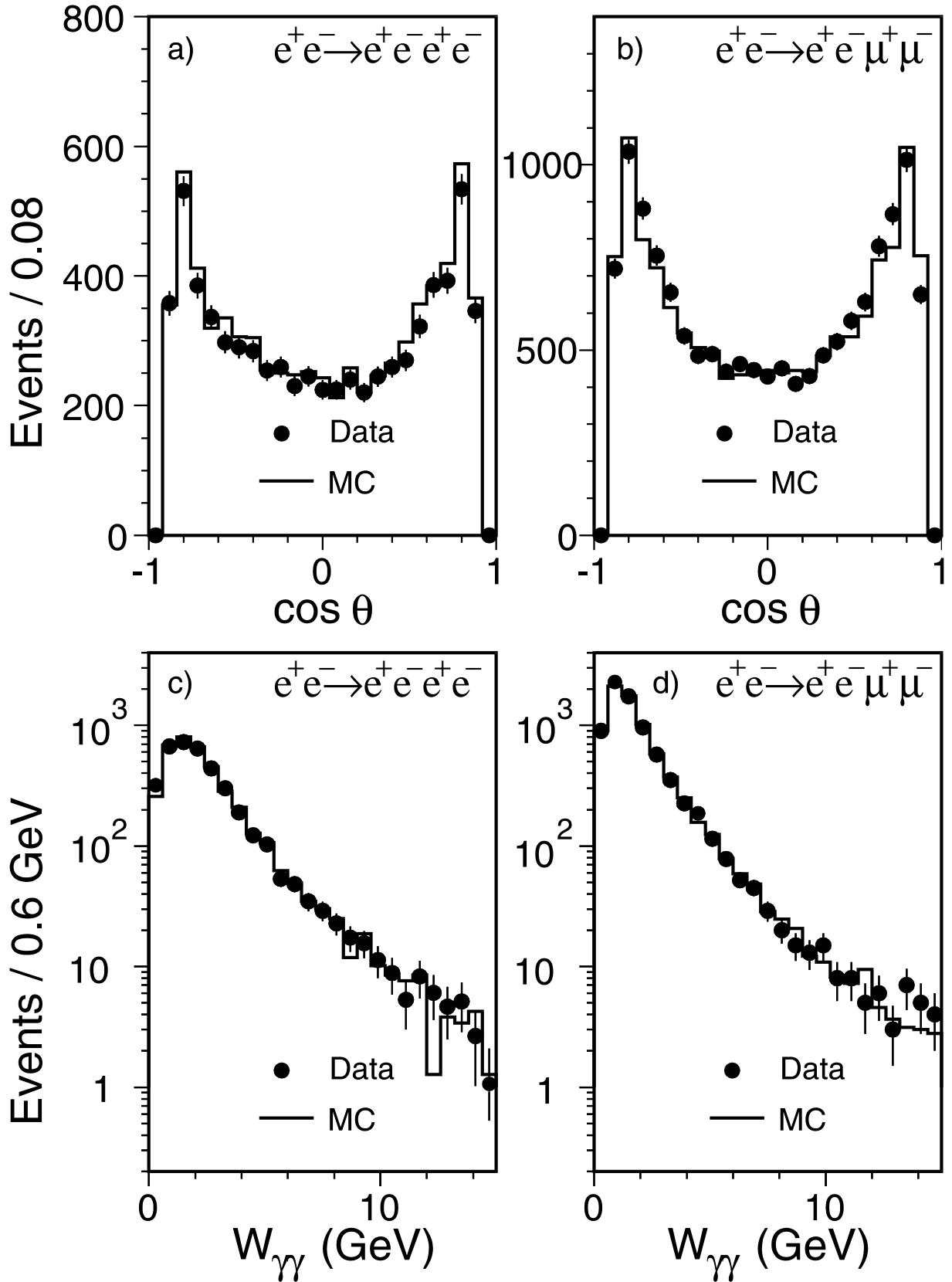


Figure 2: Comparison of data and Monte Carlo [14], normalized to the integrated luminosity, for the lepton (e or μ) polar angle and the two photon mass. The reaction $e^+e^- \rightarrow e^+e^-e^+e^-$ is in (a) and (c), the reaction $e^+e^- \rightarrow e^+e^-\mu^+\mu^-$ in (b) and (d).

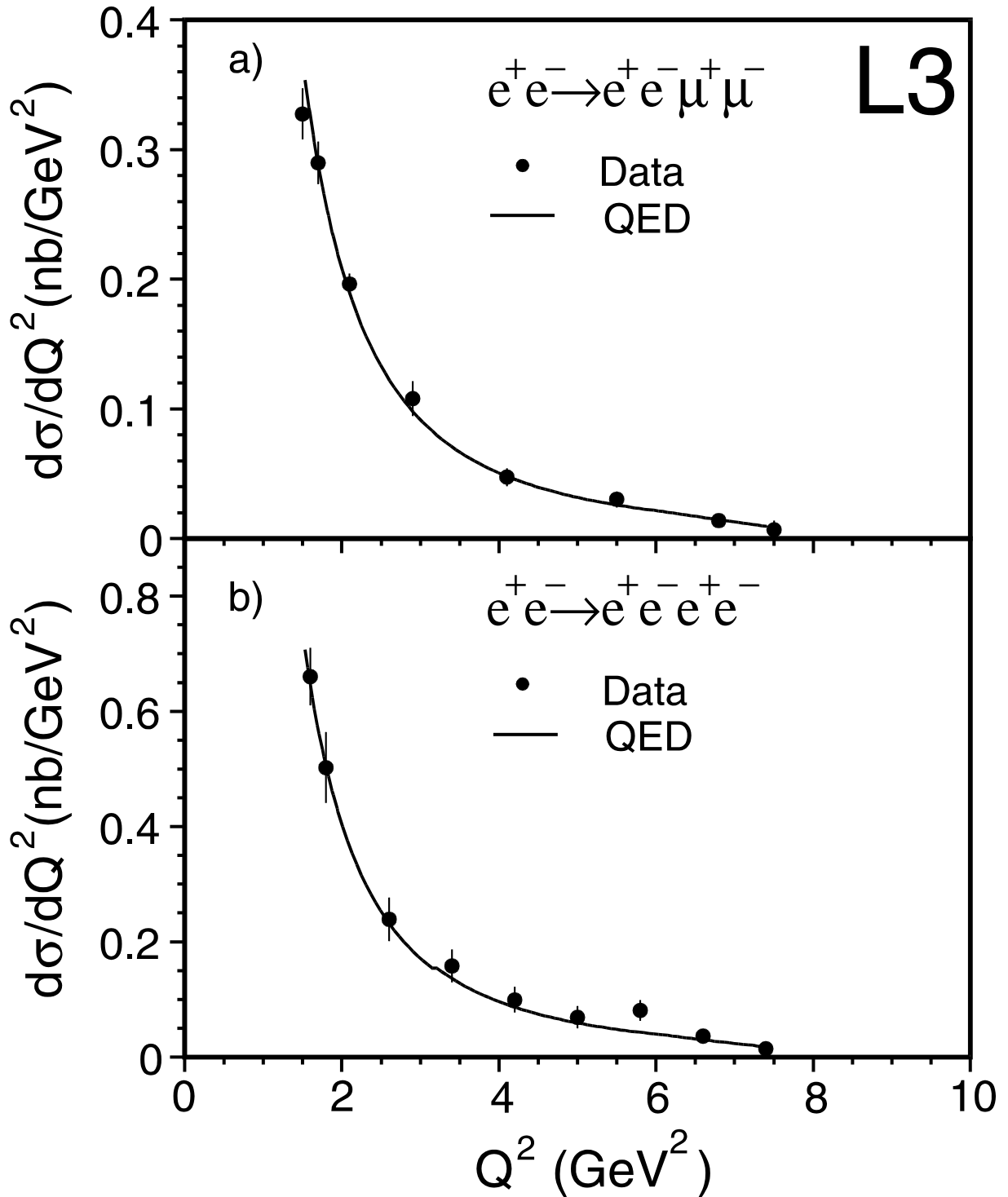


Figure 3: Differential cross section as function of Q^2 , for $W_{\gamma\gamma} \geq 0.5$ GeV, for the reactions (a) $e^+e^- \rightarrow e^+e^-\mu^+\mu^-$ and (b) $e^+e^- \rightarrow e^+e^-e^+e^-$. The QED predictions are obtained from Equation 1 and Equation 3 using a mean virtuality $\langle t^2 \rangle = 0.033$ GeV² for the target photon.

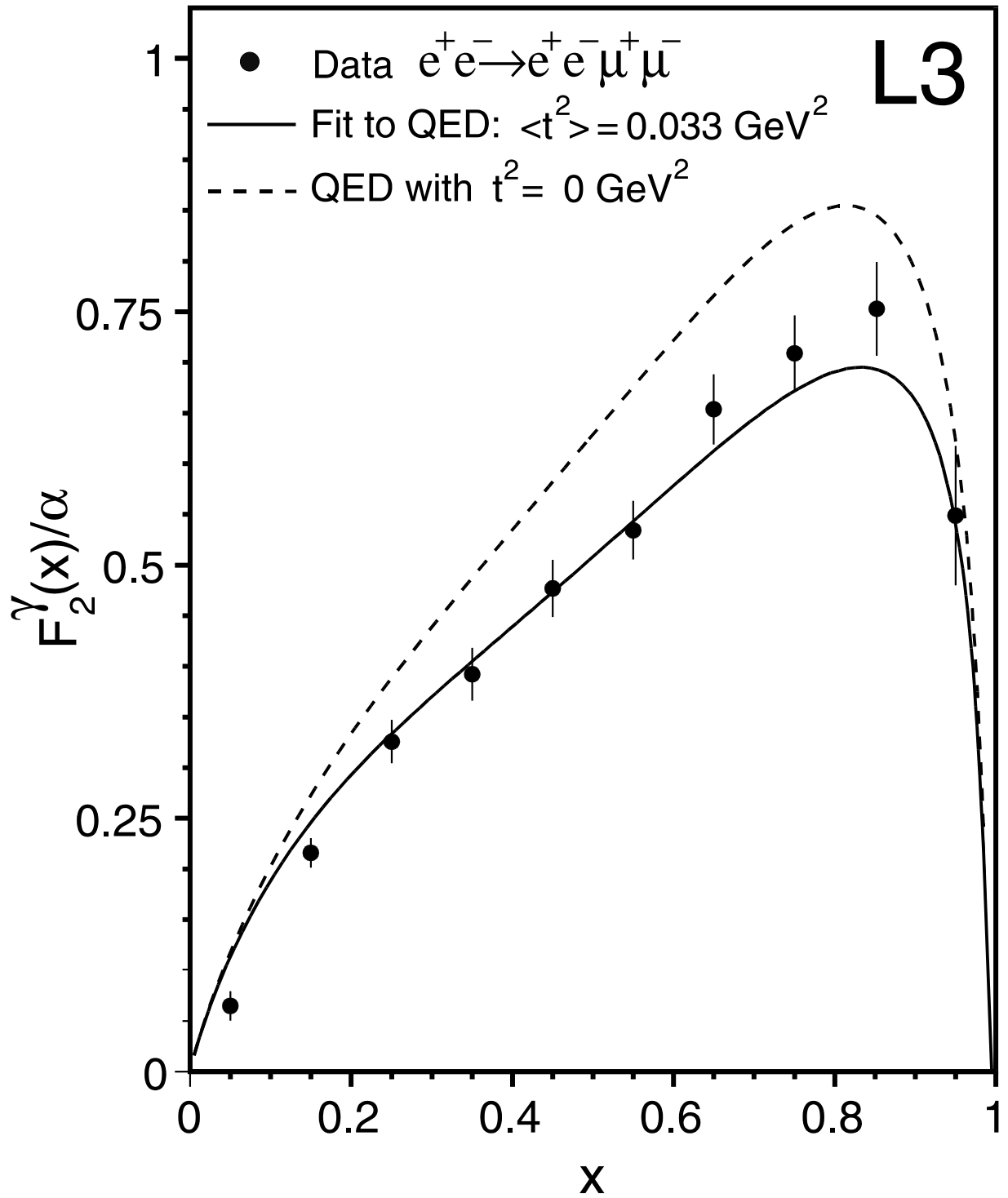


Figure 4: The leptonic structure function F_2^γ measured in the range $1.4 \text{ GeV}^2 \leq Q^2 \leq 7.6 \text{ GeV}^2$. The dashed line corresponds to QED predictions obtained from Equation 3 with $t^2 = 0$. The solid line is obtained by fitting the mean virtuality of the target photon to the data. Only statistical errors are shown, in addition there is a systematic scale uncertainty of $\pm 3.3\%$.

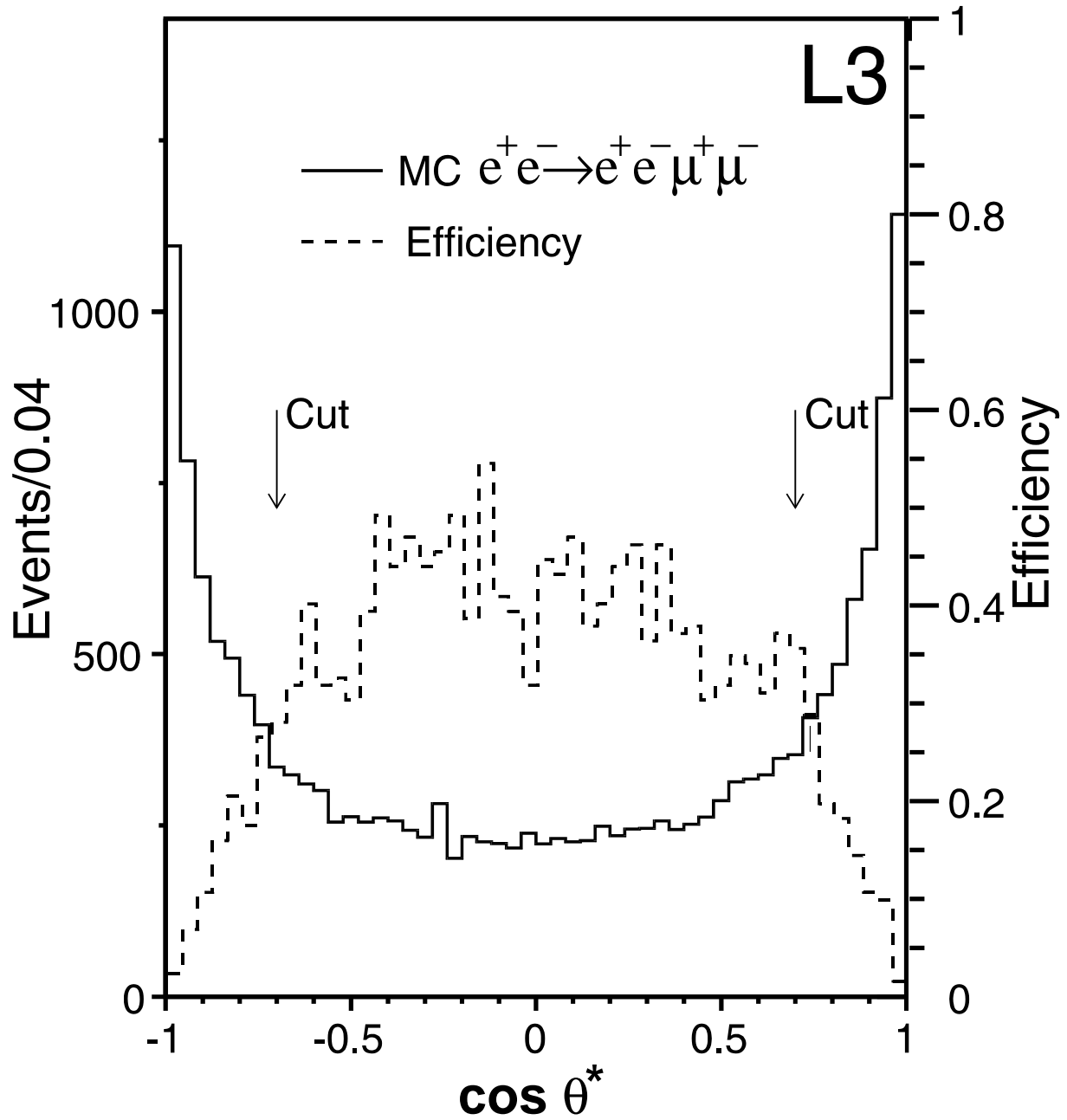


Figure 5: Monte Carlo angular distribution of $\cos\theta^*$ (solid histogram, left scale) and the corresponding selection efficiency (dashed histogram, right scale). The two arrows indicate the region used in the analysis.

$$e^+e^- \rightarrow e^+e^-\mu^+\mu^-$$

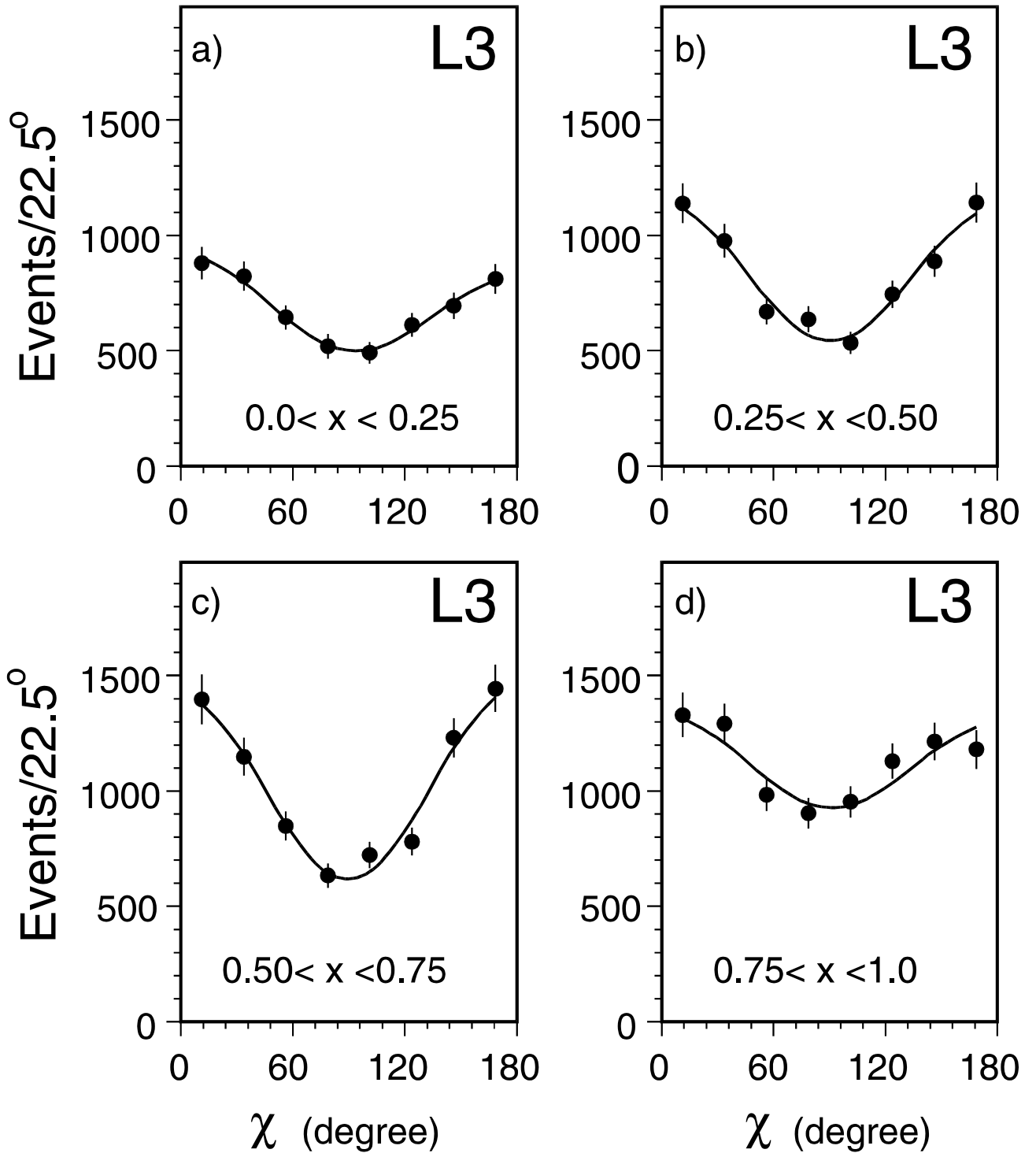


Figure 6: The μ^- azimuthal angle distribution for $|z| < 0.7$ in four intervals of x . The data are corrected for selection efficiency. The curves show the function given in Equation 7 with the value of $R_{2\chi}$ determined by a fit to the data in each x interval (see table 2).

$$e^+e^- \rightarrow e^+e^-\mu^+\mu^-$$

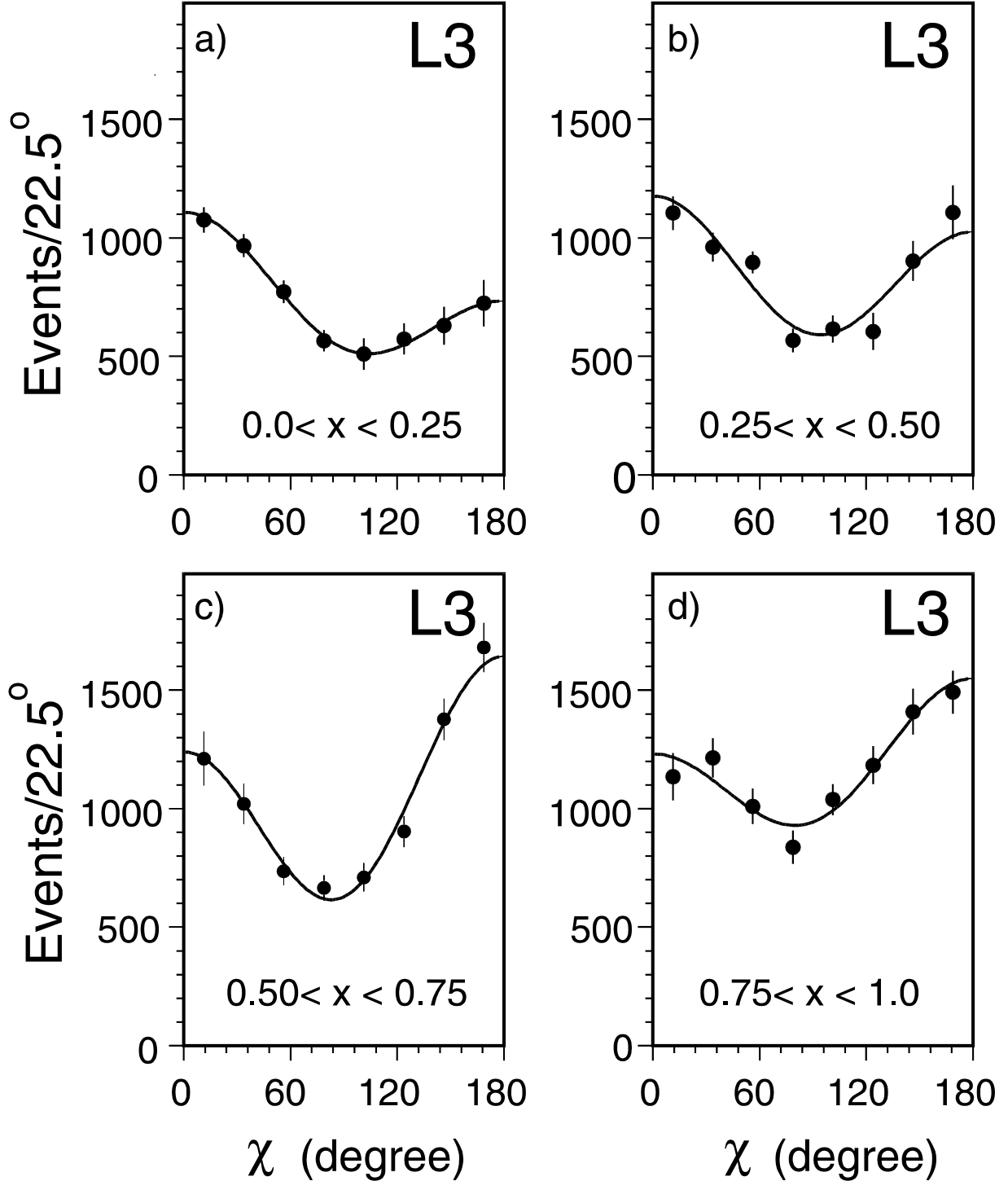


Figure 7: The μ^- azimuthal angle distribution for $-0.7 \leq z \leq 0.7$ in four intervals of x . The data are corrected for selection efficiency. The sample with $z < 0$ is added to the sample with $z > 0$ using the transformation $\chi \rightarrow \pi - \chi$. The curves show the function given in Equation 7, with the value of R_χ and $R_{2\chi}$ determined by a fit to the data in each x interval (see table 2).

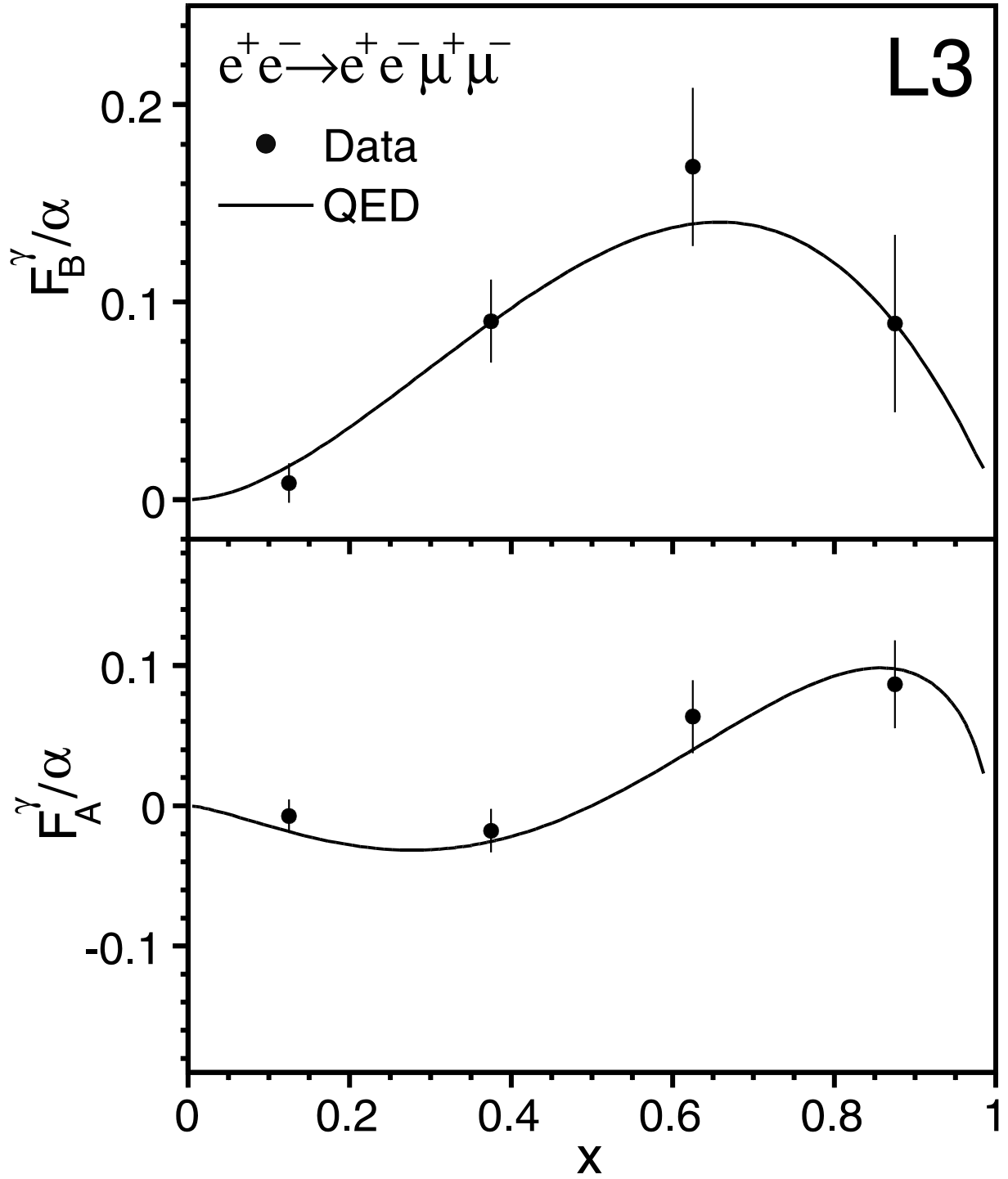


Figure 8: The leptonic structure functions F_B^γ and F_A^γ as extracted from the R_χ , $R_{2\chi}$ and F_2^γ measurements as function of x . The QED predictions from Equation 5 (see text) are superimposed on the data. The structure function F_A^γ is the weighted average between $F_A^\gamma(z > 0)$ and $-F_A^\gamma(z < 0)$. The statistical and systematic errors are added in quadrature.